UNIVERSITY OF LEEDS

This is a repository copy of *Solar thermal irradiation cycles and their influence on the corrosion behaviour of stainless steels with molten salt used in concentrated solar power plants*.

White Rose Research Online URL for this paper:
https://eprints.whiterose.ac.uk/194140/

Version: Accepted Version

Article:

Liu, Q orcid.org/0000-0002-1132-9392, Qian, J, Neville, A et al. (1 more author) (2023) Solar thermal irradiation cycles and their influence on the corrosion behaviour of stainless steels with molten salt used in concentrated solar power plants. Solar Energy Materials and Solar Cells, 251. 112141. p. 112141. ISSN 0927-0248

https://doi.org/10.1016/j.solmat.2022.112141

© 2022 Elsevier Ltd. All rights reserved. This manuscript version is made available under the CC-BY-NC-ND 4.0 license http://creativecommons.org/licenses/by-nc-nd/4.0/.

Reuse

This article is distributed under the terms of the Creative Commons Attribution-NonCommercial-NoDerivs (CC BY-NC-ND) licence. This licence only allows you to download this work and share it with others as long as you credit the authors, but you can’t change the article in any way or use it commercially. More information and the full terms of the licence here: https://creativecommons.org/licenses/

Takedown

If you consider content in White Rose Research Online to be in breach of UK law, please notify us by emailing eprints@whiterose.ac.uk including the URL of the record and the reason for the withdrawal request.

White Rose
university consortium
Universities of Leeds, Sheffield & York

eprints@whiterose.ac.uk
https://eprints.whiterose.ac.uk/

Solar thermal irradiation cycles and their influence on the corrosion behaviour of stainless steels with molten salt used in Concentrated Solar Power plants

Qingyang Liu [a,b,*] , Jiong Qian [b,c], Anne Neville [a,b] and Frederick Pessu [a,b].

a. Institute of Functional Surface, School of Mechanical Engineering, University of Leeds, Leeds, LS2 9JT, United Kingdom.

b. Jiuli Corrosion and Integrity Centre Laboratory (University of Leeds), Leeds, LS2 9JT, United Kingdom.

c. Engineering Research Centre of High-Performance Nuclear Power Pipe Forming of Zhejiang Province, Huzhou 313028, China

*Corresponding author: Qingyang Liu (mnql@leeds.ac.uk)

Keyword:

Molten nitrate salt; Isothermal; Thermal cycling; Thermal shock; Interfacial oxides; Spallation.

Highlight:

Thermal shock heating cycles during CSP operation was successfully simulated.
TS effect significantly increased material loss rate than TC and ISO conditions.
Corrosion rate under TS is increased by the spallation rate of interfacial oxides.
The evolution of interfacial oxide layers directly correlates with the rate of spallation of interfacial oxides.

Abbreviation

CSP: Concentrated Solar Power; CR: Corrosion Rate; TC: Thermal Cycling; TS: Thermal Shock; ISO: Isothermal; TES: Thermal Energy Storage.

Abstract

In this study, the corrosion behaviour of stainless steels AISI 321 and 347 in molten nitrate salt were investigated for up to 28 days. Three different thermal conditions; isothermal, thermal cycling and thermal shock, were explored to investigate the effect of the likely temperature gradients on the corrosion characteristics of AISI 321 and 347 during the operation of Concentrated solar power plants. Gravimetric corrosion analysis was combined with micro-morphology and cross-sectional analysis of the corrosion interface; using a combination of scanning/transmission electron microscopy, energy dispersive X-ray spectroscopy and X-Ray diffraction techniques, for this study. Results from corrosion rate measurements and surface characterisation show that thermal shock induces higher material degradation rate than the two other temperature profiles. Severe spallation of interfacial corrosion oxide layers was observed under thermal shock conditions other than in isothermal and thermal cycling conditions and correlated to the overall performance after 28 days. The level of spallation of interfacial oxides across the three temperature profiles investigated in this study was linked to the induced stresses from mismatch in the thermal expansion properties between the corrosion oxide layer and the substrates.

1. Introduction

The urgent need for clean and renewable sources of energy has greatly promoted the development of the solar thermal electricity in last few decades. The concentrated solar power (CSP) plant, accompanied with thermal energy storage system (TES), is the most promising energy conversion technology by transferring the abundant but intermittent solar energy into renewable, dispatchable and stable electricity [1]. This process requires the participation of solar heat as a medium to capture and store thermal energy from the sunlight to heat steam for electricity generation. Many researchers [2-4] have been investigating the metallic components, thermal storage material and the working principles of CSP plants. Mainstream commercial CSP systems are based on solar power collector technology due to its high potential efficiency, low operation cost and low environmental impact [3]. In Solar power plants, molten nitrate salts (60 wt % $NaNO_3$ and 40 wt % KNO_3) are widely served as heat transfer fluids and thermal storage material, due to its good thermal-physical properties (such as high heat capacity, high thermal conductivity, wide working temperature range, low corrosivity, high viscosity and low cost) to collect, transfer and store energy in heat collectors, heat transfer pipes and hot tanks respectively [5-7].

The operation of CSPs at the temperature $\geq 600^{\circ}C$ inevitably poses significant corrosion threats to all the metallic components in contact with molten salt. Corrosion threat to metallic components is expected to increase with the recent push towards higher temperature up to 720˚C with more aggressive salt types such as chloride and carbonate salt [8] to reduce the levelized cost of electricity (LCOE) [9]. In this case, the optimal combination of salt type and metallic materials is of vital importance for safe and stable operation of CSP to avoid any potential failure caused by potential occurrence of corrosion. Many researches on the corrosion performance of carbon/low-alloys steel, stainless steels and Ni-based alloys with different salts at different temperatures are summarized by M. Walczak [2] respectively. Updated corrosion studies [10-12] investigating different alloys resistance in solar salt by immersion and electrochemical methods have been conducted under isothermal conditions. Despite different test methods employed, almost all the results are conducted under isothermal condition and provided quick material selection guide for the combination of salt and metals.

However, in the real CSP plants, the operating conditions are more intricate and more complex due to the alternation of day/ night and even unpredictable and sharp weather change within a short period of time. In this study, we will introduce two new methodologies linked to two different temperature profiles encountered during CSP operations. These are ‘thermal cycling’ and ‘thermal shock’, which reflects the type of temperature changes that takes place during a typical CSP operation. Thermal cycling was developed to closely simulate real solar irradiation and storage cycles from the industrial scale CSP plant. It accounts for temperature profile during 12-hour peak day-time heating and 12-hour night-time cooling within heat transfer pipes or heat storage tanks [13]. In a type CSP with two-tank sensible TES, the tanks and pipes are as much as possible under isothermal conditions. However, pipes from receivers to hot tanks and to turbines / heat exchangers experience hot isothermal heating profile during available solar radiation and ‘cold’ isothermal at night (just above melting temperature). Hot tanks at daytime would store as much as possible hot salts and then pump them out to turbine to generate electricity at 6-10 pm and 7-9 am [3] (peak-consumption of electricity). Typical CSP-TES systems [3] have maximum 7-hour storage capacity of hot tanks, which would experience ‘cold’ isothermal (290°C) after running out salt stock or deep cycling (i.e. to 30°C) after drainage of salt. Literatures reporting the effect of thermal cycling on the corrosion performance in CSP plant are limited. Bradshaw [14] found that thermal cycles could moderately increase the corrosion rate of stainless steels, while B.Li [15] investigated how thermal cycling affects the thermal stability and properties of mixed carbonate salts. Previous study [13, 16] also reported that the thermal cycling reduces the mass loss and corrosion rate by slowing down the corrosion kinetics of the reactions. The thermal cycling / thermal shock should generally involve chemical degradation / dissolution of molten salt [9, 13] and mechanical degradation [17-19] of material under this study, which could further bring more complexity in a CSP fields.

It is well established that, the availability of consistent solar irradiation could significantly affect the electric energy generation capacity and efficiency of CSPs. According to CSP operations and maintenance experience, the receiver pipe panels are expected to experience a rapid temperature drop by a few K per second from working temperature to ambient temperature (25°C) by the weather changes like dark clouds and strong winds. These are common scenarios (described as “thermal shock”) in real tower power plants constructed at northwest of China, where extreme weather attacks frequently. Under this circumstance, the engineers have to cut off the solar irradiation from mirrors (heliostats) in advance to take away the heat on the surface of the receiver pipe panels. The threat posed by irregular thermal shocks on material integrity is significant and always contributes to severe deformation, causing material failure and leading to the shutdown of the CSP system and causing significant economic loss. In other words, the deformation and explosion of receiver pipes induced by thermal stresses and thermal shock are fatal to the whole plant because those expensive parts are highly metallurgical precise, and difficult to repair. Also researchers affirmed that the spallation behaviours of the oxides layer [20] were attributed to the stresses mismatch [21] between the bulk material and oxide layers due to difference in the thermal expansion coefficient and elastic modulus of it [22].

There are currently limited studies on effect of thermal shock on the corrosion mechanism and performance of metallic components molten salt. This further introduces more complexities to the corrosion mechanisms in comparison to thermal cycling and isothermal temperature profiles. In this study, the corrosion characteristics and performance of stainless steels (AISI 321 and 347) are investigated under isothermal, thermal cycling and thermal shock condition in molten nitrate salt with air as cover gas for up to 28 days. Thermal shock in this study is simulated between 565 and 30°C, while thermal cycling is simulated between 565 and 290°C. The methodology and results in this study could provide an updated guideline for the characterization and selection of the materials for use in CSP plants.

2. Description of Experimental System

2.1 Samples and salt preparation

Solar salt (60 wt. % $NaNO_3$ and 40 wt. % KNO_3) was selected for this study due to its wide application in CSP plants. The salt was weighed and mixed to achieve the required ratio and placed in a box glove with inert gas for 2 days. Then the salt was moved to the furnace to dry at 120 for 24 hours. Details of salt purity and preparation procedure can be found in previous publication [13] and supplementary file.

The materials used in this study were AISI 321 and AISI 347 austenitic stainless steels, and the composition of these alloys is provided in Table 1. The as-received pipes were supplied by Zhejiang JIULI Hi-tech Metals Co., Ltd China. Samples with dimension of 23mm*13mm*3mm were wire-cut from the wall of seamless pipes, as shown in Figure 1. The test samples were wet grind to 1200 grit with silicon carbide (SiC) paper and followed by polishing with 9 µm, 6µm, 1µm and 0.25 µm diamond paste. Polished samples were then degreased with acetone and deionized water, respectively, following by hot-air drying. The initial dimensions and mass of coupons were recorded using a micrometre and analytical balance (0.01mg, Ohaus Analytical Plus balance, New Jersey, United States).

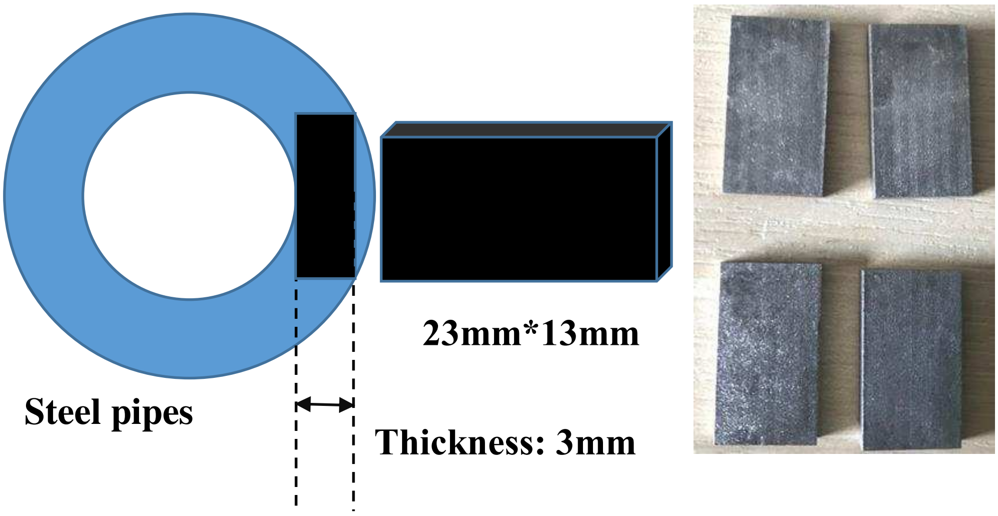

Figure 1 Geometry of samples obtained from the pipes and the dimensions.

Table 1 alloy composition of 321 and 347 (wt%).

Alloy	C	Mn	Si	P	Cu	Cr	Ni	**Ti**	**Nb**	Mo	**Fe**
AISI 321	0.018	1.44	0.519	0.0347	-	17.33	9.24	0.225	-	-	Bal.
AISI 347	0.049	0.95	0.402	0.026	0.11	17.35	9.65	-	0.656	-	Bal.

2.2 Experimental procedure

The test samples were placed in individual crucibles and covered with dried nitrate salt mixture in accordance with the specification of ISO 17245:2015 [23]. The tests commenced after transferring each sample-containing crucible into the muffle furnace, as shown in Figure 2 (a) and (b). The tests were conducted under isothermal, thermal cycling and thermal shock condition in air for 7 days, 14 days and 28 days respectively, according to the time-temperature profile shown in Figure 3 (a) and (b).

The temperature fluctuation between 290 and 565°C every 12 hours in thermal cycling is designed to replicate as closely as possible the real-time cycle between daytime 12-hour peak heating and night-time 12-hour cooling. The heating and cooling rate for thermal cycling is set as 10°C/min. 565°C was set as isothermal temperature and peak temperature for thermal cycling and thermal shock, below which the salt mixtures can remain stable. Most of the pipes and cold tanks are kept above the melting temperature of the salt (220°C) to prevent blockages, so 290°C was chosen for thermal cycling in this study.

For thermal shock, the temperature of the samples drops significantly from 565°C in molten salt to 30°C in air within 10 minutes to simulate the drainage process of molten salt in the receiver pipes during the rapid cooling process that occurs as a result gust of cold wind and cloudiness, that cuts off the supply of solar irradiation. The thermal shock samples were taken out of salt-containing crucibles by tongs and kept in air at room temperature (30 ± 2˚C and relative humidity of 50 ± 5%) for 30 minutes. Afterwards, the samples were re-immersed into liquid salt immediately to exaggerate the effect of thermal shock [14]. This process was repeated once a day at a fixed time to compare the results with isothermal and thermal cycling test.

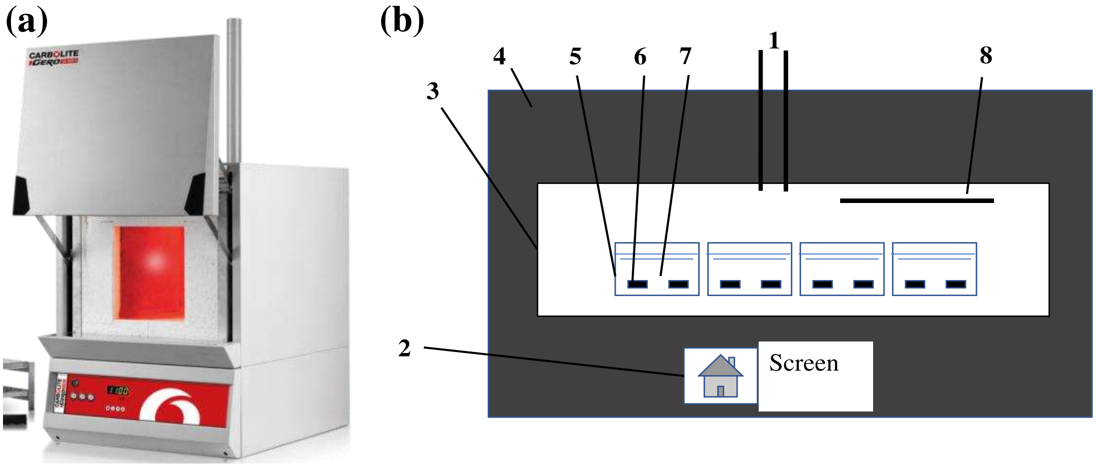

Figure 2 The structure of muffle furnace whole (a) and part (b) for corrosion experiment: 1-Chimney; 2 Control unit; 3-test chamber; 4-heating unit; 5-crucible; 6-specimen; 7-molten salt; 8thermocouple.

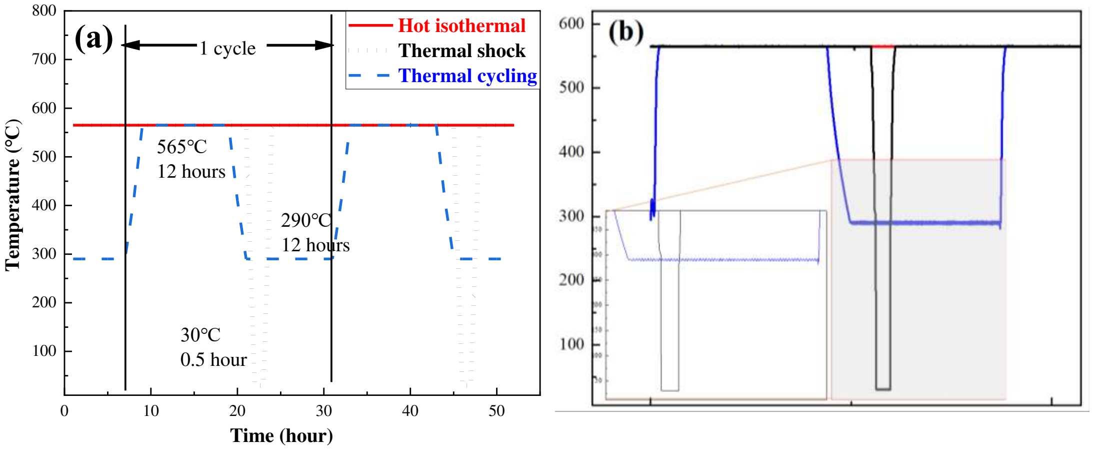

Figure 3: (a) the designed and (b) oven recorded time-temperature profile of isothermal immersion, thermal cycling and thermal shock

2.3 Microstructural characterization

A Bruker D8 X-ray diffractometer was used for X-ray diffraction analysis of alloys to identify the corrosion product on the corroded surface using monochromatic Cu Kα radiation (λ=1.5418 Å). It should be mentioned that the samples were cleaned with deionized water for 2 minutes to remove the residue salt on the surface. XRD patterns were collected in the 2θ range from 10° to 90° with a 1.5°/min scan rate. The surface morphology and cross-sections analysis of samples were investigated using a Zeiss optical microscope (OM) (Axio Imager 2) and Carl Zeiss EVO MA15 scanning electron microscope (SEM). The SEM was integrated with an Oxford Instruments Aztec Energy dispersive X-ray (EDX) system with an 80mm X-max SDD detector which provided secondary and backscattered imaging, EDX elemental mapping and line scans. The incident beam voltage of 20 keV was employed and working distance of 8-9 mm.

The samples for cross-section analysis were embedded in epoxy resin before mechanically grinding and polishing to the mirror surface without scratches. Then the low energy Ir sputtering for coating on cross-sectional samples is to enhance the conductivity in SEM-EDX system. Advanced surface characterisation using transmission electron microscopy (TEM) was performed on AISI 321 samples after 1 week to investigate and understand the early stages of interfacial oxide formation kinetics under all test conditions. TEM samples were cut from the tested samples using Focused Ion Beam (FIB) operated at between 30 and 5 kV and beam currents between 5 and 0.1 nA. The surfaces were coated with platinum before micro-machining and thinning of the samples to ~ 100nm thick for TEM analysis. TEM was performed using FEI Titan Themis Cubed X-FEG (300kV) fitted with a high angel annular dark field detector and a Gatan OneView 16 Megapixel CMOS digital camera.

2.4 Mass loss measurement and corrosion rate calculations

Every 5 samples of AISI 321 and 347 were retrieved from each crucible after 7 days, 14 days and 28 days, and cleaned in deionized water and acetone to remove the residual salt on the surface. Three of the samples were used for mass change / corrosion rate measurements and the other two were used to characterise the corrosion products by SEM-EDX, XRD and other morphological characterisation tests.

Weight loss before and after immersion test were calculated via **Equation 1** and thus corrosion rate was estimated by **Equation 2** after removal of corrosion products on the surface according to the ASTM G1-03 [24] and British standard BS EN ISO 8407:2014 [23]. More detailed experimental procedure of cleaning the corroded sample and the calculation of corrosion rate can be found in previous publication [13].

$$\frac{\Delta m}{S} = \frac{m_0 - m_1}{S} \qquad \textbf{Equation 1}$$

$$CR(\mu m/y) = \frac{87600\,\Delta m}{\rho\, S\, t} \qquad \textbf{Equation 2}$$

3. Results and discussion

3.1 Mass loss and corrosion rate measurements

The time dependence of mass loss or corrosion rate can be used to explain the process and mechanism of corrosion reaction. Pieraggi [25] introduced parabolic kinetics to illustrate the corrosion/oxidation performance; that mass loss increase linearly with the square root of time and described by the following parabolic law:

$$\Delta \mathrm{m} = k_p t^{1/2} + A_p \qquad \textbf{Equation 3}$$

Where k_p is the parabolic rate constant (mg/(cm^2·h$^{1/2}$)), t is the exposure time (h), A_p is the intercept term (mg/cm^2). Figure 4 shows the descaled mass loss with the square root of time for AISI 321 and 347 under different thermal conditions, from where we can observe that the mass loss for all samples increase with increase in exposure time. It is also observed from Figure 4 and Figure 5 that samples from thermal cycling tests recorded the lowest mass loss and corrosion rate values while samples from thermal shock showed the highest mass loss and corrosion rate values.

In comparison to isothermal corrosion over 28-days, mass loss samples from thermal shock tests were observed to increase by ~35.7% for AISI 321 (from 2.33 mg/cm^2 in isothermal to 3.157 mg/cm^2 in thermal shock after 28 days), and ~285.7% for AISI 347 (from 1.40 mg/cm^2 to 5.40 mg/cm^2 after 28 days). Similarly, mass loss of samples from thermal cycling tests was observed to decrease by 51.7% for AISI 321 (to 1.125 mg/cm^2), and 29.7% for AISI 347 (to 0.9845 mg/cm^2) compared with that from isothermal test after 28 days. It is shown that the AISI 321 and 347 have similar profile of mass loss and corrosion rate changes with time under isothermal and thermal cycling condition. To have a better comparison between the three different thermal conditions investigated in this study, the time scale of isothermal, thermal cycling and thermal shock was normalised based on the result of mass loss after 672-hour (4 weeks) immersion test. For AISI 321: 100h ISO – 207.0h TC (total time) – 73.8h TS – 103.5h TC (hot time only), for AISI 347: 100h ISO – 143 h TC (total time) – 25.9h TS – 71.5 h TC (hot time only). It is worth mentioning that the normalised time for thermal cycling was calculated by ‘total time’ and ‘hot time’ respectively to give insight into the temperature dependency of corrosion kinetics. The samples for AISI 321 would be immersed for 207 hours and 74 hours under thermal cycling and thermal shock condition to obtain the same level corrosion of 100-hour equivalent time for isothermal sample. Meantime, the AISI 347 samples were expecting much less equivalent time for thermal cycling and thermal shock than AISI 321. The detailed normalisation process was shown in the supplementary files.

We concluded that AISI 321 depicts better corrosion resistance to temperature fluctuation, i.e. thermal cycling / shock than AISI 347. The addition of titanium (AISI 321) and niobium (347) to steel composition is efficient to reduce the sensitization (IGC) and lead to different corrosion resistance by preferential precipitating the (Ti, Nb)C [26] rather than Chromium carbide. We assume that the titanium is a more efficient stabilizing agent than niobium based on the conditions explored in this study [27].

In addition, the mass loss increases linearly with square root of immersion time. This is presented in Figure 4. Parabolic terms; k_p and A_p were obtained by fitting of mass loss against square root of time according to **Equation 3**. The values of k_p and A_p listed in Table 2. The parabolic rate constants k_p of AISI 321 and 347 increase with change in temperature profile of the immersion tests this order; thermal cycling < isothermal< thermal shock. This observation correlates with the observation mass loss in Figure 4 and suggest the influence of the changing temperature profiles on the kinetic of corrosion of AISI 321 and 347 in molten nitrate salts. Also, the values of coefficient of determination (R^2) for the fitted curves are greater than 0.75, indicating the good degree of fitting.

Despite the increase of mass loss over time, the corrosion rate is observed in Figure 5 to decrease with time for AISI 321 and 347 under Isothermal and thermal cycling conditions. The corrosion rate of AISI 321 and 347 after 28-day or 28-cycle immersion test were 38.2 and 22.7 μm/yr or 18.5 and 15.9 μm/yr. From weight loss analysis in this study, and in reference to the industry accepted threshold of 20 μm/yr of corrosion rate to provide a 30-year lifetime service for CSP plants [28], AISI 321 and 347 can be considered under thermal cycling condition for 30 years or isothermally employed for 15 years. However, the result in this study is limited to the 4 weeks of exposure time. It is still unclear how the materials would behave with an extended exposure time beyond the 4 weeks considered in this study. For thermal shock condition, the mass loss significantly increase between 7 and 14 days of immersion test, and then decreases again after 28 days. The higher corrosion rate of AISI 347 than 321 shows the unique complexity introduced by the cycles of thermal shock.

As already established in a previous study [16], the range of temperature used for the cooling phase (290°C) during thermal cycling, and the long residence time during this period is believed to help to slow down the kinetics of corrosion, oxide formation, and thereby supress material loss rate. This intermittent cooling effect could also have similar effect on the aggressiveness of the molten salt chemistry [13]. Spallation behaviours were more likely to occur on samples from isothermal tests than from thermal cycling. However, the effect of thermal shock is believed to rapidly undermine the integrity and adherence of the corrosion oxide layers to continuously leave the fresh metal exposed to molten salt, and thus leading to an increase of corrosion rate. The detailed evidence and analysis are discussed in the next section of this paper.

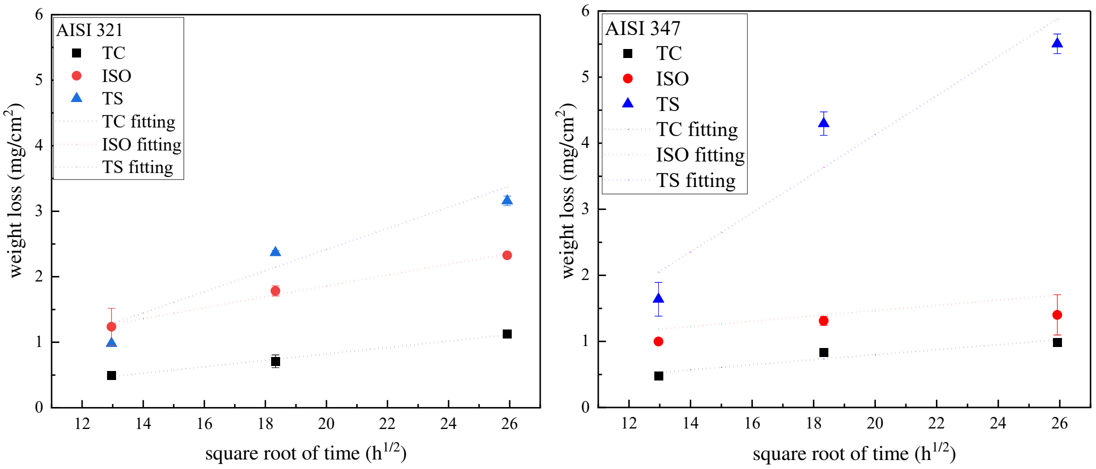

Figure 4 Mass loss of AISI 321 and 347 under different thermal conditions. Error bars represent the deviations in the mass loss measurement. Fitting curves are also presented with dot line in the figure.

Table 2 Results of linear fitting of weight loss.

Alloy	Condition	kp (mg/(cm^2·h$^{1/2}$))	Ap (mg/cm^2)	R^2
321	TC	0.0491	-0.16	0.993
	ISO	0.0833	0.1934	0.990
	TS	0.1612	-0.8082	0.847
347	TC	0.0381	0.0364	0.897
	ISO	0.0398	0.6692	0.843
	TS	0.2957	-1.7854	0.786

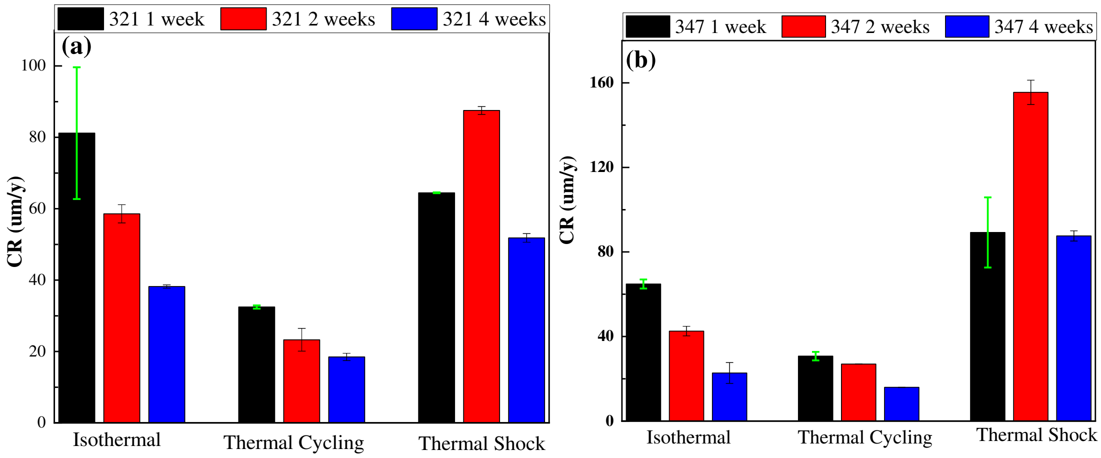

Figure 5 Corrosion rate of AISI 321 and 347 under different thermal conditions, error bars were also provided.

3.2 XRD analysis

XRD measurements were performed on the corroded surface of samples before they are embedded in resin to characterise the evolution of the chemical footprint of interfacial corrosion oxides at various immersion times for the three temperature profiles. As shown in Figure 6 (a, c and e), the main corrosion products formed on the AISI 321 are iron oxide (Fe_2O_3), iron chromium spinel ($FeCr_2O_4$), sodium ferrite ($NaFeO_2$) and chromium oxide (Cr_2O_3), regardless of the thermal profile. Similar corrosion products chemistries were observed on the surface of AISI 347 shown in Figure 6 (b, d and f). Cr_2O_3 and $FeCr_2O_4$ are known to be more dense and protective when formed as inner layers, and are capable of providing substantial corrosion barrier to molten salts [29]. Porous and less protective oxide layers of $NaFeO_2$ and Fe_2O_3 were found as outer layer of the corrosion product. Data on the distribution and relative thickness of the interfacial corrosion oxides are presented and discussed in the next section of this paper.

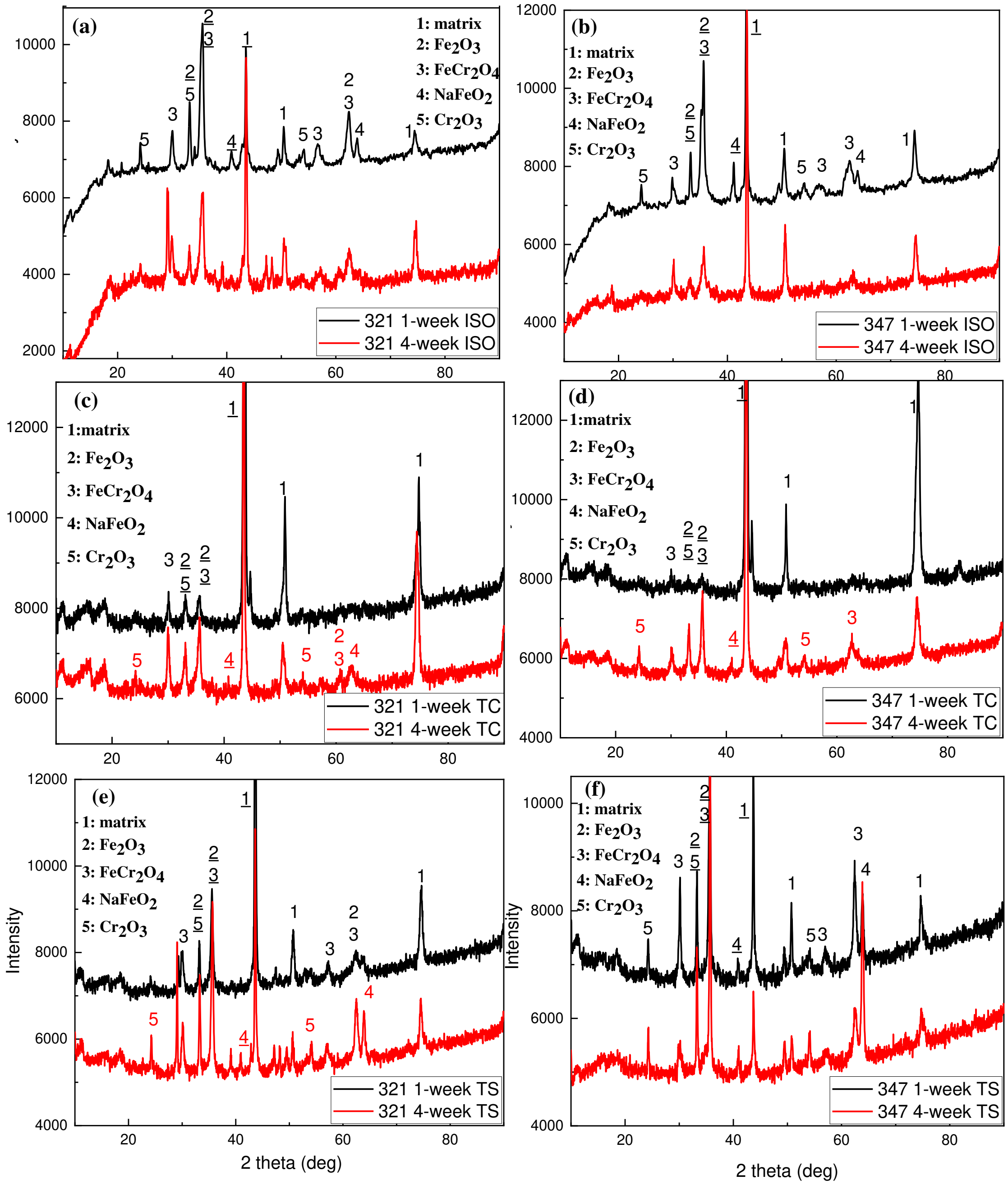

Figure 6 XRD patterns of AISI 321 and AISI 347 after 1-week and 4-week under thermal cycling, isothermal and thermal shock condition, respectively (the number with underline represents the 100% intensity of corresponding product).

3.3 Characterisation of corrosion oxide layer

After the immersion corrosion test in molten salt, different types of oxide layers were found and were believed to offer variable levels of protection to base metal against further infiltration of molten salt on the surface of samples. The formation process and distribution of corrosion products are important to improve on current understanding of the corrosion mechanisms. The morphologies and complementary EDX results of AISI

321 and AISI 347 under different thermal conditions are shown in Figure 7 and Figure 8 respectively.

It is evident that the surfaces became more coarse and were covered by corrosion oxide layers with time for isothermal condition (see Figure 7 (a) and (b) for AISI 321, and Figure 8(a) and (b) for AISI 347 after 1- and 4-weeks exposure respectively). Iron oxide was the main corrosion products on the surface after the 1-week with 12 wt% Cr contents in Figure 7 (a). This indicates the existence of protective Cr_2O_3 and/or $FeCr_2O_4$ oxides with help from XRD result. After 4 weeks, the Fe and Na were found to be higher, while the Cr content reduced significantly in the outer oxide layers as identified from EDX analysis (P4 and P5) in Figure 7 (b). This indicates the increase in the formation of porous and non-protective Fe_2O_3 and $NaFeO_2$ outer oxide layers (See Figure 7 b). Inner oxides layer, with a higher Cr content, was exposed to molten salt after spallation of outer layer. Similar observation was recorded for AISI 347 in Figure 8 (a) and (b), and EDX analysis in Figure 8 (region P3 and P4).

Under thermal cycling conditions, the samples exhibited only a slight difference in terms of the overall surface features on the corroding interface after 1-week and 4-weeks. Referring to Figure 7 (c) and (d), and Figure 8 (c) and (d) for AISI 321 and AISI 347 respectively, it is evident that the corrosion oxide layers are more resilient and continuous across the entire surface. This is an indication of more stable oxide layers, with little or no spallation. From the result of EDX analysis in Figure 7 and Figure 8 (c) and (d) and XRD results in Figure 6 (c) and (d) , we can confirm that the main corrosion oxides formed on stainless steels under thermal cycling conditions samples are Fe_2O_3 and mixture oxides of Fe and Cr (Cr_2O_3 and $FeCr_2O_4$). The overall effect of lower material loss rate (Figure 5) and surface features under thermal cycling conditions than isothermal is related to the effect of long residence time at lower temperature (290°C) in the heating cycle. The duration of the intermittent cooling process in the heating cycles has the direct effect of suppressing the kinetics of corrosion, oxide formation and rate of spallation. All of these three processes collectively influence the overall corrosion behaviour of materials under thermal cycling condition.

Figure 7 (e) and (f), and Figure 8 (e) and (f), presents the SEM and EDX results for test under thermal shock condition for AISI 321 and 347 sample. Although corrosion oxide layers are observed in localised regions on the surface, there is also evidence of substantial spallation after 1 week (Figure 7 (e) for AISI 321 and Figure 8 (e) for AISI

347) due to the thermal shock resulting from the temperature profile. The coverage area of corrosion oxide layer reduces after 4 weeks due to severe spallation by extending periods of thermal shock (See Figure 7 (f) and Figure 8 (f). After 1-week thermal shock test for AISI 321, the inner surface (region P12 and 13) was observed with higher Cr and Ni content than the exfoliated of outer layer (region P14 and 15) in Figure 7 e. This observation is also the same for AISI 347 in Figure 8 (e) and (f). At other regions of the sample, there is evidence of dense, adherent and protective inner layer. This is likely to be a mixture of oxides of Fe and Cr, such as Fe_2O_3, Cr_2O_3 and $FeCr_2O_4$ (region P12 and 13 Figure 7 e). Referring to evidence shown in region P14 and 15 from EDX analysis, it is clear that there is an outer Fe and Na rich oxide layer. This is likely to be the porous and poorly adherent layers, identified as Fe_2O_3 and $NaFeO_2$ by XRD spectra in Figure 6 (e) and previous publications [13, 16]. This outer layer is prone to being spalled off; particularly as a result of the substantial thermal amplitude the samples are subjected to under thermal shock conditions. It is also evident from Figure 7 (e) and (f), that majority of this outer layer has been lost to the thermal shock effect. After 4-week immersion test under thermal shock condition, severe spallation of corrosion layers was observed. The extend test duration also provided opportunity for reformation of initially spalled off oxide layers. This is shown in Figure 7 (f) that pieces of outer layer of $NaFeO_2$ and Fe_2O_3 left after spallation are shown in region P19 for AISI 321. Evidence of Cr and Fe rich inner oxide layer after spallation is shown in region P18. Most of these outer oxide layers are shown in Figure 7 (f) to have spalled off due to thermal shock and inner Cr-enriched layer is prone to dissolve into molten salt. After spallation of initially formed layers, new oxide mixtures of Fe, Cr and Na are formed on the site of region P16 and P17 in Figure 7 (f). Similar observation to AISI 321 was also recoded for AISI 347 after 4-week test under thermal shock conditions. Evidence of scattered particles identified as $NaFeO_2$ formed on superficial oxide layers can be seen at region P15 and P16 in Figure 8 (f).

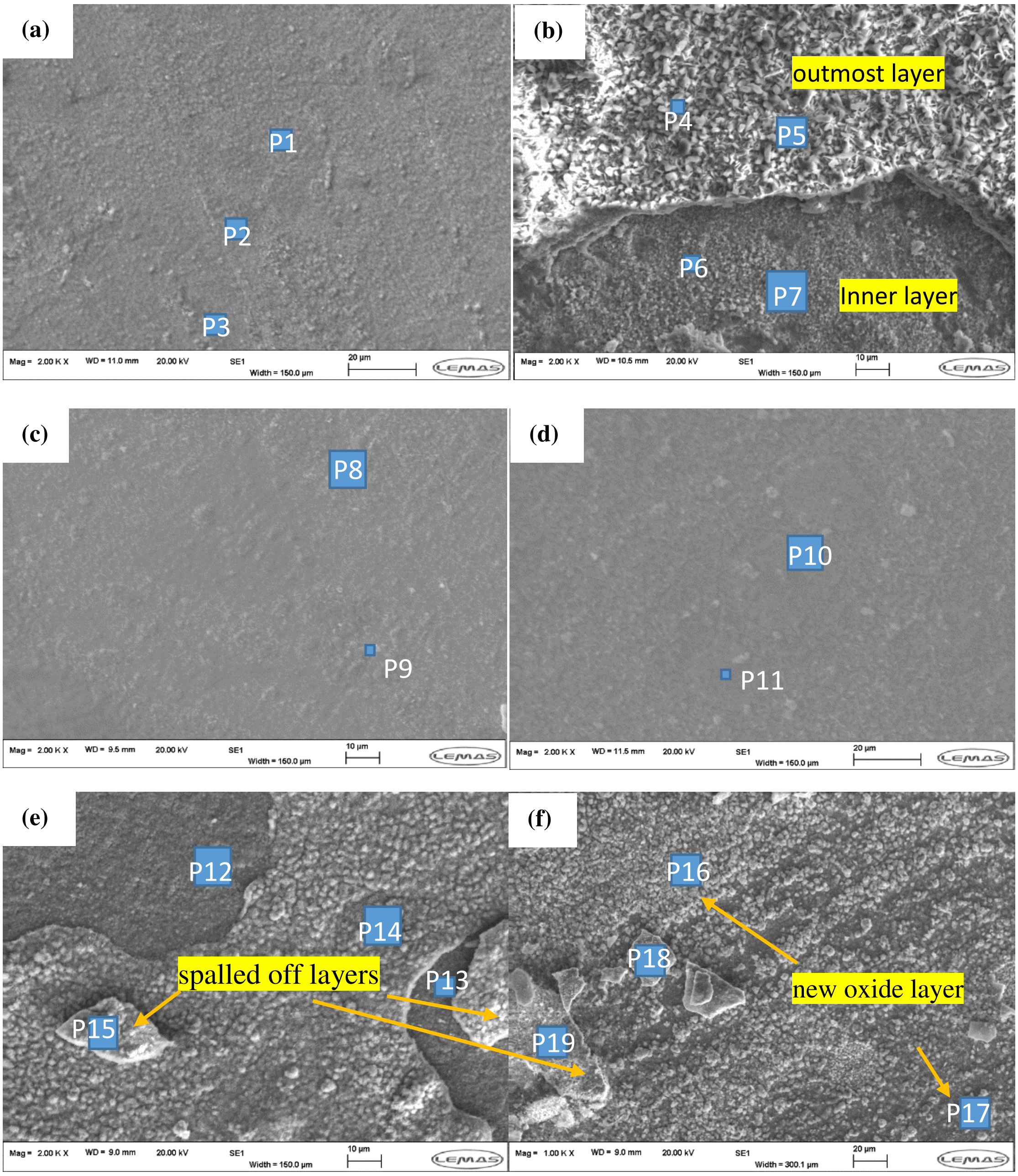

Element in wt %	Fe	O	Cr	Na	Ni
P1 P2 and P3	60.3 ± 0.2	18.3 ± 1.2	12. ± 0.9	0.1	-
P4 and P5	59.4 ± 1.2	30.0 ± 0.6	0.8 ± 0.3	9.4 ± 0.8	-
P6 and P7	68.0 ± 1.4	25.2 ± 0.4	3.7 ± 1.4	0.1	-
P8 and P9	63.3 ± 1.0	16 ± 1.5	10.7 ± 0.2	-	8.7 ± 0.3
P10 and 11	64.2 ± 3.0	24.7 ± 1.3	7.4 ± 0.6	-	2.5 ± 0.2
P12 and 13	65.3 ± 2.5	23.4 ± 2.1	6.5 ± 1.0		2.0
P14 and 15	66.2 ± 4.5	20.3 ± 3.1	1.6 ± 0.2	2.1± 0.2	
P16 and 17	62.1 ± 1.0	23.6± 0.4	2.2 ± 0.5	7.2± 1.2	-
P18 and 19	55.7± 0.2	23.5 ± 3.2	1.1 ± 0.6	5.3 ±1.2	-

Figure 7 SEM surface observation of the oxide scales formed on AISI 321 after (a) 1-week Isothermal; (b) 4-week Isothermal; (c) 1-week Thermal cycling; (d) 4-week

Thermal cycling; (e) 1-week Thermal shock; (f) 4-week Thermal shock immersion test in molten nitrate salt. Table below shows the EDX data for regions.

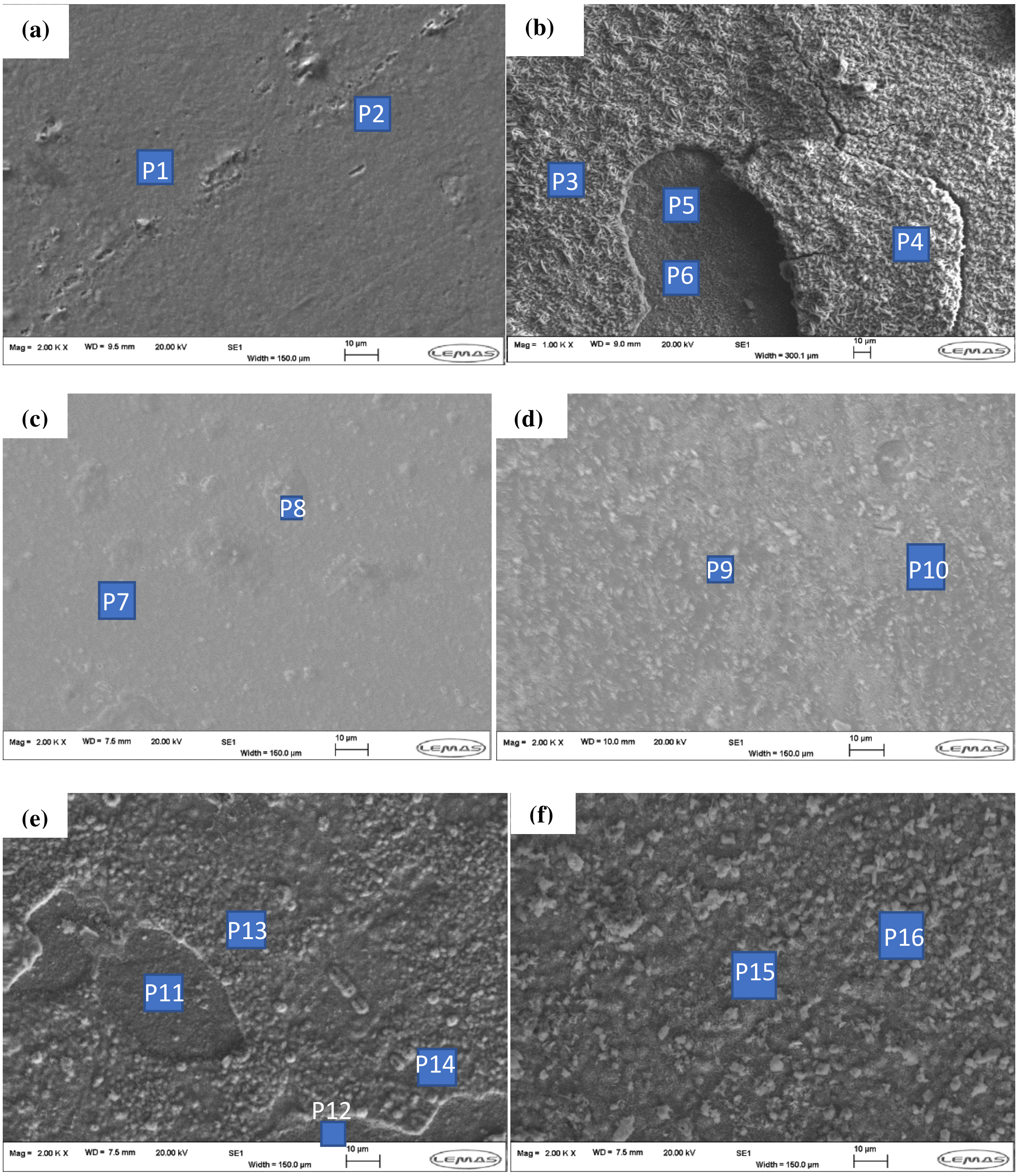

Element in wt %	Fe	O	Cr	Na	Ni
P1 and P2	66.2± 3.2	17.4 ± 0.5	12.6 ± 0.5	0.1	8.5± 0.5
P3 and P4	62.5 ± 0.7	25.7± 0.9	1.1± 0.1	10.8 ± 0.1	0.01
P5 and P6	70.8 ± 0.5	22.8 ± 0.3	3.8 ± 0.4	0.42	1.63
P7 and P8	68.5 ± 3.2	10.4 ± 3.5	8.1± 0.5	0.1	5.5± 0.5
P9 and P10	61.5± 1.7	24.9± 0.6	7.0± 0.6	3.5 ± 0.6	0.9± 0.2
P11 and P12	66.1 ± 1.4	20.6 ± 2	8.0± 0.2	1.35	0.1
P13 and P14	68.5± 2.1	23.7± 2.2	2.1± 0.1	2.7 ± 0.5	0.1
P15 and P16	65.5± 2.4	22.3± 0.9	1.7± 0.1	5.5 ± 1.6	0.1

Figure 8 SEM surface observation of the oxide scales formed on AISI 347 after (a) 1-week Isothermal; (b) 4-week Isothermal; (c) 1-week Thermal cycling; (d) 4-week

Thermal cycling; (e) 1-week Thermal shock; (f) 4-week Thermal shock immersion test in molten nitrate salt.Table below shows the EDX data for regions.

Cross – Sectional Analysis

Cross-sectional analysis was conducted to examine the corrosion layer formed during the immersion test. As shown in Figure *9* for AISI 321, there are no indication of intergranular corrosion. From the SEM analysis above, it is evident that uniform corrosion driven by rate of spallation of interfacial oxide layers is the primary mode of corrosion attack for the conditions and duration explored in this study. Referring to Figure *9* and Figure 10 for AISI 321 and AISI 347 respectively, oxide layer with a mixture of oxides of Fe and Cr; likely Cr_2O_3 and Fe_2O_3 (confirmed by XRD in Figure 6) was found as an interfacial oxide layer under isothermal (after 1 week) and thermal cycling (after 1 and 4 weeks) condition (see Figure 7 (a), (c) and (d)). The thickness of the corroded layer are 2 and 4 µm after thermal cycling and 3.5 and 9.3 µm after isothermal test, as annotated in Figure *9*. For AISI 347, the thickness of the oxide layer formed under isothermal condition was ~2.5 µm, which increases with exposure time to around 12.5 µm after 4 weeks in a similar trend to AISI 321. A thin corrosion oxide layer formed after thermal cycling immersion test in Figure 10 (c) and (d). From the embedded line scan, Fe_2O_3 was the main oxide formed.

Double oxide layers was found on the 4-week isothermal samples in Figure *9* (b) for AISI 321. This double oxide layer with an outer $NaFeO_2$ layer was also observed after 4 weeks on AISI 347 (See line scan in Figure 10 (b)). This interface consisted of outer (Fe, Na)-rich oxides and inner (Cr, Ni)-rich oxides. This observation corroborates with the XRD pattern in Figure 6 and the SEM Images in Figure 7 and Figure 8.

Outer Fe_2O_3 and inner Cr_2O_3 layer were observed on AISI 321 after 1-week thermal shock with uniform thickness of 3 µm (See Figure *9* (e). Similar oxide layer with a uniform thickness of 4 µm was observed for AISI 347 as shown in Figure 10 (e). After 4 weeks test under thermal shock condition, a large size detached oxide particle was observed above a continuous corrosion oxide layer. Quite of corrosion oxides spalled off during the test, and thus cannot be detected in the cross-section observation. This correlates the spallation process and believe to drive the oxide removal mechanism with the surface observation in Figure 7 (f) and Figure 8 (f) for AISI 321 and 347 respectively. Underneath this detached oxide particle of $NaFeO_2$, consist of two thin layers of Fe_2O_3 (intermediate layer) with higher Fe content and inner mixture of oxides of Fe and Cr.

The spallation of corrosion oxide layer was also observed on Figure 10 (e) for AISI 347 after 1-week thermal shock test. In this case, the detached layer was identified as Fe_2O_3 which prevent the dissolution of Cr-compound by other researchers [30, 31] under isothermal conditions. It is clear that the Fe_2O_3 layer has been undermined by the thermal shock heating cycles. It is probable that after the spallation of the protective layers, the inner Cr-oxides layer is become exposed for dissolution into salt due to the solubility of chromium compounds in nitrate salt [30, 31]. Newly formed Fe_2O_3 layer was formed again beneath the spalled layer as a potential barrier for the inner mixture oxide of Cr from dissolution into molten salt [9, 16]. After 4-week thermal shock test, superficial oxide mixtures of Na and Fe were believed to be $NaFeO_2$ and Fe_2O_3 from results of XRD and SEM-EDX. This outer oxide layer is about 3 µm thick and has been shown to be porous and loose in previous study [32, 33]. However inner mixture of $(Fe, Cr)_2O_3$ is 2 µm thick, and is likely to continue to grow due to unhindered molten salt induced corrosion activities at the metal – molten salt interface without the protection from the outer corrosion oxide layers. This is shown in Figure 10 (f).

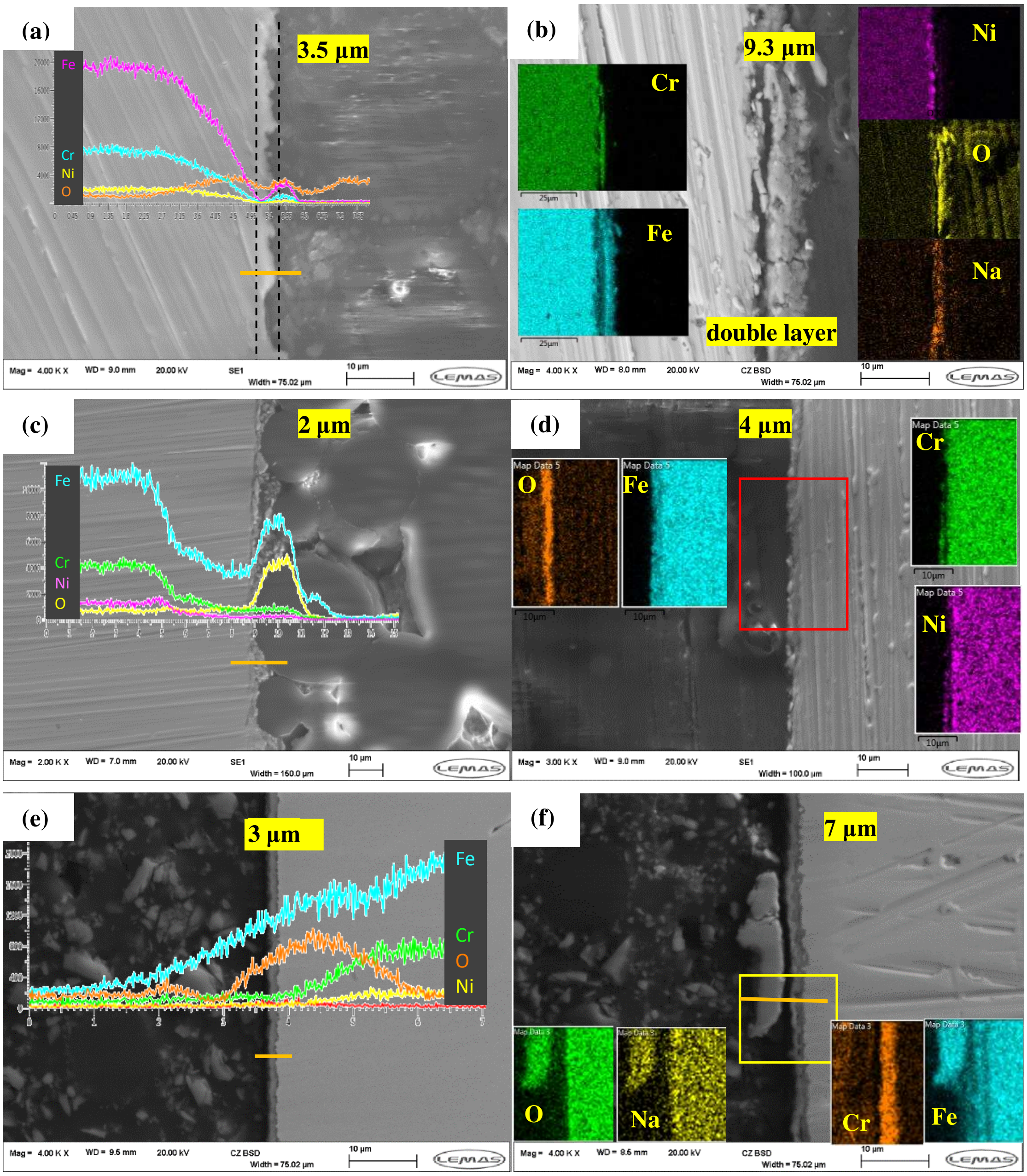

Figure 9 cross-sectional images of AISI 321 by SEM-EDX after (a) 1-week Isothermal; (b) 4-week Isothermal; (c) 1-week Thermal cycling; (d) 4-week Thermal cycling; (e) 1-week Thermal shock; (f) 4-week Thermal shock immersion test in molten nitrate salt.

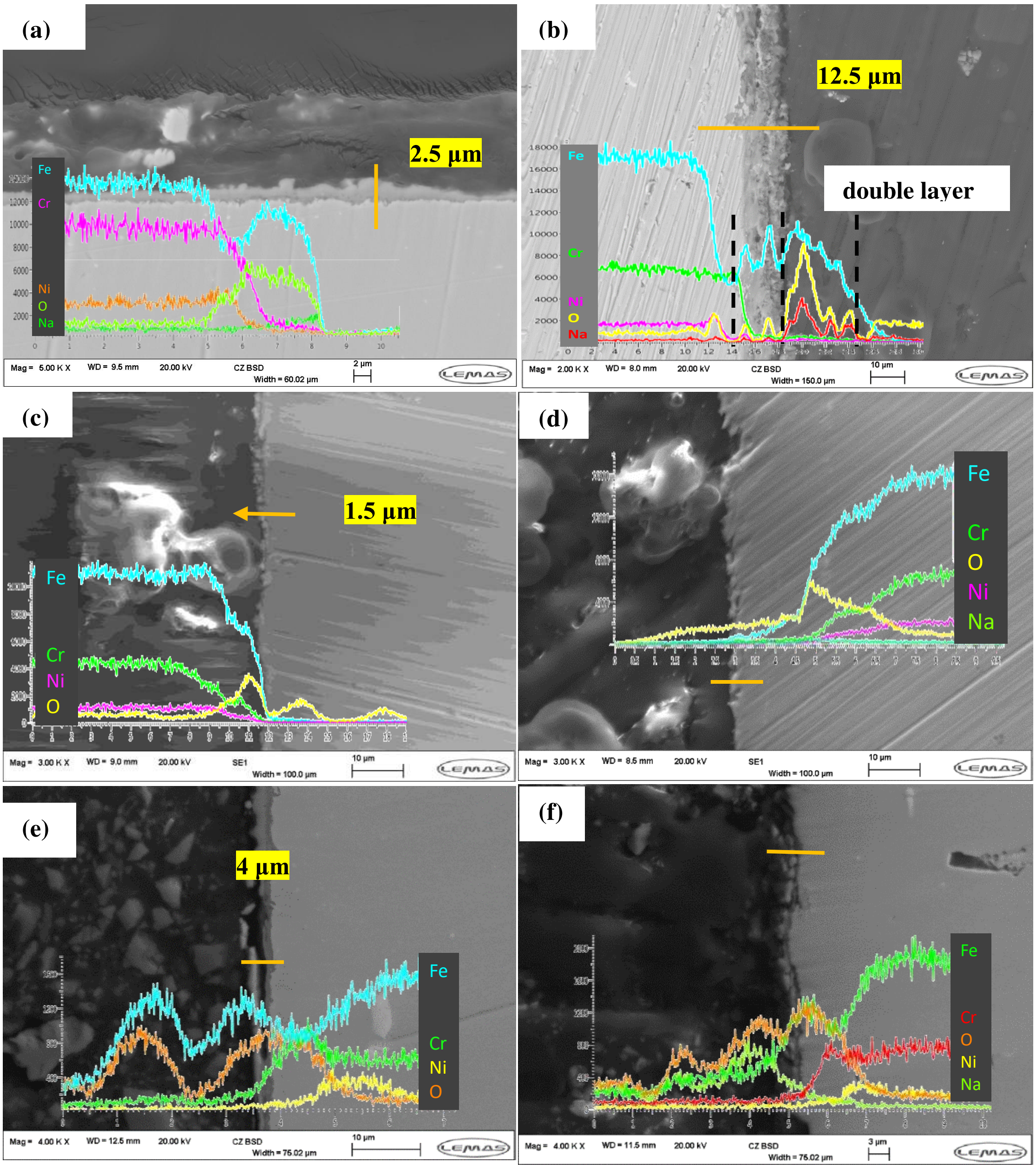

Figure 10 SEM-EDX profile of AISI 347 after (a) 1-week Isothermal; (b) 4-week Isothermal; (c) 1-week Thermal cycling; (d) 4-week Thermal cycling; (e) 1-week Thermal shock; (f) 4-week Thermal shock immersion test in molten nitrate salt.

3.4 Corrosion behaviour and the Evolution of Interfacial oxide Layers

In order to better understand the evolution and characteristics of the interfacial oxide layers on stainless steel in molten nitrate salt under different thermal conditions, a combination of FIB, SEM and TEM was used to characterize the interfacial oxide layers. This is shown for AISI 321 after 1 week in Figure 11 for isothermal, thermal cycling and thermal shock test conditions.

After 1-week test under all thermal conditions, relatively thin oxide layers (below 3 µm) were observed on the AISI 321 surface. Figure 11 (a) shows the cross-sectional image, corresponding EDX mapping images, and SEAD patterns for samples after of 1-week test under isothermal condition. A 1.37-µm outer layer was formed on the surface, which was identified as mixture of Fe_2O_3 and $NaFeO_2$ by patterns for annotated area a1 and EDX mapping in Figure 11 (a). An intermediate oxide layer of about 0.64 µm thick, was found as Cr-enriched layer in region (a2). The TEM pattern shows the intermediate layer was mainly Cr_2O_3 and $FeCr_2O_4$ spinel, which is known to be protective against further corrosion. A 0.2-µm (Cr, Ni) enriched layer was also found as an inner layer adjacent to the bulk material. This (Cr, Ni) rich inner oxide layer is believed to have been formed at an earlier early stage in the corrosion process.

For samples after thermal cycling tests, the thickness of the oxide layer was about 0.87 µm in Figure 11 (b), consisting of a 0.33-µm outer $NaFeO_2$ and Fe_2O_3 layer in region (b1), a 0.16-µm middle mixed (Cr, Fe) oxide layer at region (b2), and a porous mixture of Cr_2O_3, $FeCr_2O_3$ and Fe_2O_3 layer at inner layer in region (b3). The formation of the porous inner layer is linked to the dissolution of the Cr-enriched inner layer into solar salt at initial stage and later formed Fe-enriched layer above it could hinder the chromium removal from the substrate. The relatively lower thickness of the layer is linked to the repressed kinetic of the corrosion reaction and oxide formation by intermittent cooling period at low temperature (290°C) and shorter residence time at peak temperature (565°C) during thermal cycling test when compared to isothermal test condition.

The corrosion layers formed on samples from thermal shock test exhibited multi-layer structure. A 0.38-µm needle like layer; identified as $NaFeO_2$ and Fe_2O_3 was observed as the outmost surface. The middle layer in region (c2) was identified as Fe_2O_3 and inner layer identified as a mixed oxide layer of (Cr, Fe) in form of Cr_2O_3 and $FeCr_2O_4$ spinel. It is worth noting that a 73 % reduction in thickness of outer layer from isothermal to thermal shock was observed, which correlates inversely with significantly higher weight loss results from thermal shock test than isothermal test (Refer to Figure *9* (a1) and (c1)).

From the mass loss results, we can say that higher corrosion rate of thermal shock samples led to a more corroded surface and thicker corrosion layers. The SEM surface observation confirmed that. But the cross-section of thermal shock samples show lower thickness of interfacial oxide layers than isothermal ones, which is not consistent with the mass loss results and surface observation. The FIB- HRTEM results shows a thickness of 0.38-µm and 1.37-µm outer Fe_2O_3 / $NaFeO_2$ layer for thermal shock and isothermal samples respectively, a thickness of 0.99-µm and 0.84-µm inner Cr_2O_3 layer were also observed . From the discussion above, we can say that the outer Fe-based layers of thermal shock have not survived due to enhanced spallation during the immersion test. The thermal stress and the corresponding frequency under thermal shock will cause the interfacial oxide layers to spall off faster leading to higher mass loss and lower thickness of interfacial oxide layers. In general, the multi-layered corrosion products formed on the surface of stainless steels always exhibited an inner Cr-enriched layer $(Fe, Cr)_2O_3$, which was considered as initially formed passive layer. Dense inner layer of Cr_2O_3 and $FeCr_2O_4$ as observed in this study are capable of being adherent to substrate, and provide good protection for material against the alloy element diffusion [13]. The dissolution of Cr_2O_3 into solar salt results in Fe_2O_3 were found to be the primary corrosion oxides, and the existence of inner soluble Cr-enriched layers indicates the outer Fe_2O_3 layers are served as barrier in preventing solar salt penetration [31]. Fe_2O_3 forms as an outer layer but potentially transforms into $NaFeO_2$ and is spalled off from the surface depending general thermal operating cycles.

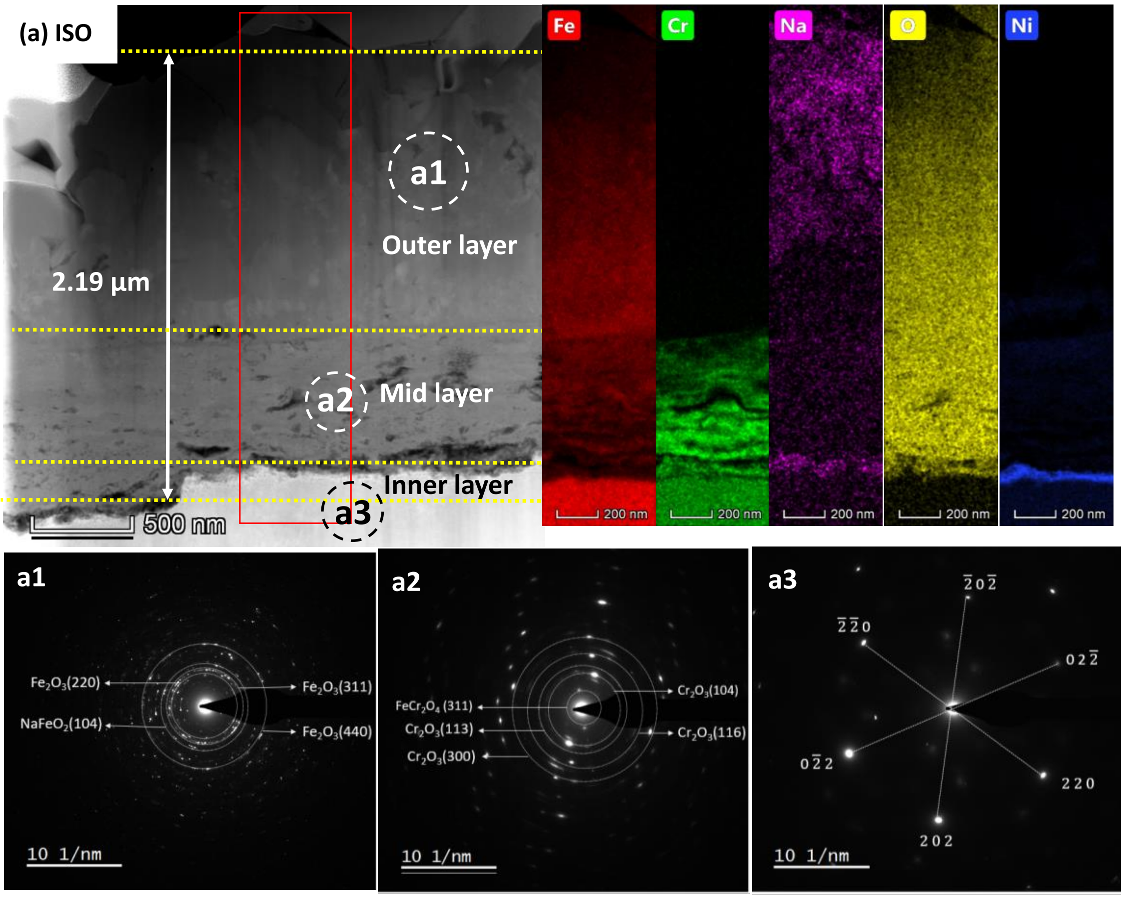
(a) ISO
2.19 µm
a1
Outer layer
a2
Mid layer
Inner layer
a3
500 nm
Fe
Cr
Na
O
Ni
200 nm
a1
Fe_2O_3(220)
$NaFeO_2$(104)
Fe_2O_3(311)
Fe_2O_3(440)
10 1/nm
a2
$FeCr_2O_4$ (311)
Cr_2O_3(113)
Cr_2O_3(300)
Cr_2O_3(104)
Cr_2O_3(116)
10 1/nm
a3
$\bar{2}0\bar{2}$
$\bar{2}\bar{2}0$
$02\bar{2}$
$0\bar{2}2$
220
202
10 1/nm

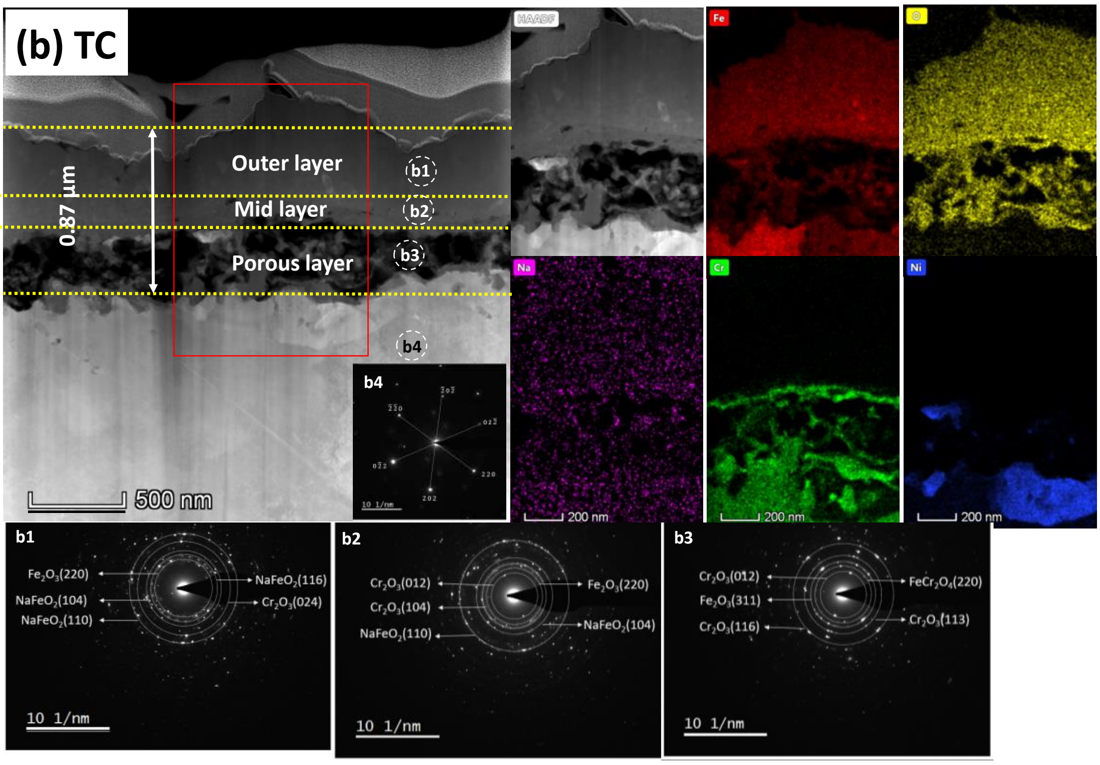
(b) TC
0.87 µm
Outer layer
Mid layer
Porous layer
b1
b2
b3
b4
500 nm
b4
10 1/nm
HAADF
Fe
O
Na
Cr
Ni
200 nm
b1
Fe_2O_3(220)
$NaFeO_2$(104)
$NaFeO_2$(110)
$NaFeO_2$(116)
Cr_2O_3(024)
10 1/nm
b2
Cr_2O_3(012)
Cr_2O_3(104)
$NaFeO_2$(110)
Fe_2O_3(220)
$NaFeO_2$(104)
10 1/nm
b3
Cr_2O_3(012)
Fe_2O_3(311)
Cr_2O_3(116)
$FeCr_2O_4$(220)
Cr_2O_3(113)
10 1/nm

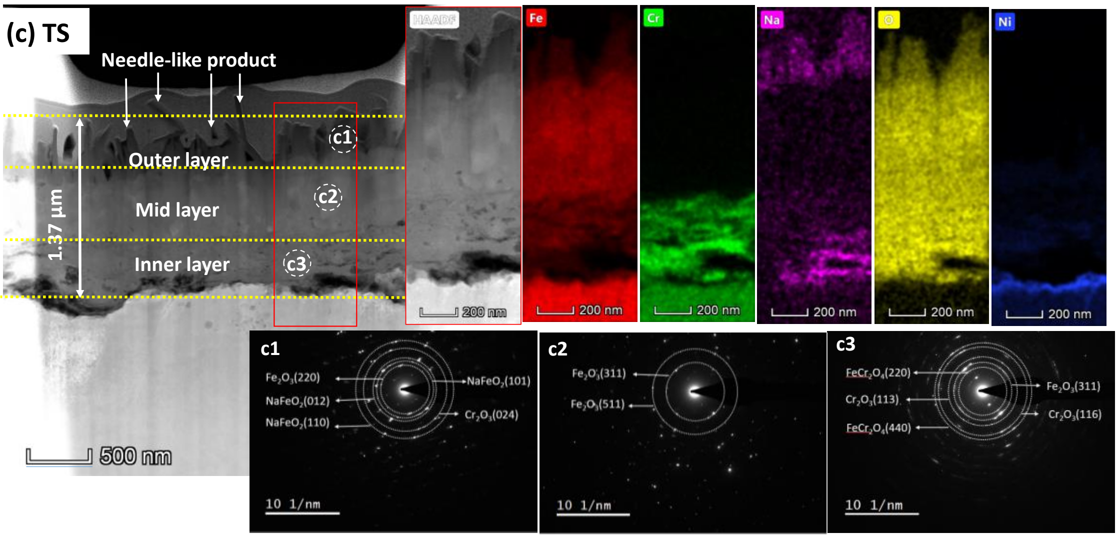

Figure 11 HRTEM images of samples after (a) 321 1-week isothermal (b) thermal cycling and (c) thermal shock and its corresponding EDX mapping and SAED patterns

3.5 Interfacial Oxide Formation Mechanism, Evolution and Stability in Relation to Oxide spallation and Overall material loss.

While results [33, 34] published recently and from this study have shown a measured rate of material degradation for AISI 321 and 347 in molten nitrate salt, the occurrence of spallation of outer oxide layer due to the thermal stress under thermal shock condition further accelerates corrosion kinetics and increases the rate of material loss. Therefore, an understanding of the mechanism of formation, evolution and behaviours of interfacial corrosion oxides is critical to better understand the corrosion mechanism of AISI 321 and 347 in molten nitrate salt under different thermal conditions as observed in this study.

Firstly, the passivation and corrosion resistance of stainless steels rely on the formation of thin and dense Cr_2O_3 and $FeCr_2O_4$ directly at the steel surface, protective properties of which can be further improved by alloying with Ni and Mo [2]. The formation reactions of Cr_2O_3, Fe_2O_3 and $FeCr_2O_4$ are shown in ***Equation 4*** - **Equation 6**. However the Cr_2O_3 and Fe_2O_3 have a complete range of solubility across all composition range [35]. With the known solubility of Cr compounds in molten nitrate salt, Cr_2O_3 and $FeCr_2O_4$ could be found at the inner region of corrosion layers, identified by XRD spectra in Figure 6.

$$2Cr + 3O^{2-} \rightarrow Cr_2O_3 + 6e^- \qquad \textbf{Equation 4}$$

$$FeO + Cr_2O_3 \rightarrow FeCr_2O_4 \qquad \textbf{Equation 5}$$

$$2\mathrm{Fe} + 3O^{2-} \leftrightarrow Fe_2O_3 + 6e^- \qquad \textbf{Equation 6}$$

$$O_2 + 4e^- \leftrightarrow 2O^{2-} \qquad \textbf{Equation 7}$$

The formation of Fe_2O_3 identified in this work occurred due to the oxidizing nature of nitrate salt with oxidizing species like NO_2^- and O^{2-} from decomposition of solar salt [10]. In addition, the oxygen in air can play a major role in accelerating oxidation as shown in ***Equation 7*** [31]. The research [31] also found that hematite occupied the middle region of corrosion scales in AISI 304 stainless steel, maintaining its inner protective chromium oxide and limiting chromium dissolution from metals [36, 37]. With increase of immersion time or temperature, the decomposition of nitrate to nitrate becomes more favourable [9, 13]. The relatively more protective Fe_2O_3 outer layer is converted to non-protective $NaFeO_2$ and accelerate the corrosion process. Ahmed [31] also found $NaFeO_2$ on stainless steel after exposure to KNO_3 –$NaNO_3$ eutectic and offered the following formation mechanism. Consequently, $NaFeO_2$ formed on the top surface of the corrosion layers.

$$NaNO_2 \leftrightarrow Na_2O + NO + NO_2 \qquad \textbf{Equation 8}$$

$$\frac{1}{2}\mathrm{Fe}_2O_3 + \frac{1}{2}Na_2\mathrm{O} \leftrightarrow \mathrm{NaFe}O_2 \qquad \textbf{Equation 9}$$

Corrosion of AISI 321 and 347 alloy is known to follow a parabolic law at 565°C in molten salt, indicating the oxidation process was controlled by ion diffusion through the oxide scales [38]. Therefore, thermodynamic and kinetic analysis on interfacial oxide scales; typically composed of Fe_2O_3, Cr_2O_3 and/or $FeCr_2O_4$ can help to better understand oxide stability and evolution [16].

The potential oxide forming corrosion reactions and the corresponding Gibbs free energy of formation of oxides on the surface of stainless steels during oxidation process are listed in Table 3. The change of Gibbs free energy of formation of the oxides was obtained by following **Equation 10** [39].

$$\Delta G = \Delta G^{\theta} + RT\, ln(\frac{(\alpha_O)}{(\alpha_M)(pO_2)^{1/2}}) \qquad \textbf{Equation 10}$$

ΔG^{θ}: standard Gibbs free energy of formation (25˚C, 1 atm); T: temperature in Kelvin; p_{O2}: partial pressure of oxygen in Pa, which was assumed to be 0.21 from other study [40]; R: gas constant 8.3145 $J \cdot K^{-1} \cdot mol^{-1}$. α_O and α_M represent the activity of the oxide and the metal. α_O is 1; α_M can be approximately obtained by atomic concentrations.

Cr_2O_3 is believed to be preferentially formed due to the lowest ΔG value (~ -1018 kJ/mol) at 565˚C for stainless steels. Considering the solubility of chromium compounds in nitrate salt [30], other oxides starts to formed once average Cr concentration was lower than a critical value (N_{Cr}*) [41]. Afterwards, the Fe-based oxides starts forming at this stage. FeO is known to form at temperature over 1000°C [22] and Fe_xO_y tend to form at temperatures below 570°C [40]. According to ΔG values of Fe_xO_y in Table 3 and the diffusivity order of metallic ions in chromia ($D_{Fe} > D_{Ni} > D_{Cr}$) [42], Fe_3O_4 and Fe_2O_3 starts to form to provide a level of protection against further Cr dissolution from the substrate. This oxidation process is controlled by ionic diffusion. The outward diffusion of Fe in the Cr_2O_3 and high affinity of Fe to oxygen resulted in formation of (Fe, Cr) oxides mixture [16]. As shown in this study, Fe_2O_3 preferentially forms as the most outer layer of the interfacial oxide layers shield inner Cr-oxide layer from aggressive molten salts. Meanwhile, it is worth noting that Fe_2O_3 tended to convert to $NaFeO_2$ with increase of exposure time and temperature, thus causing the corrosion interface to lose its outermost shielding layer increase overall material loss.

Table 3 Gibbs free energies of formation of oxides in stainless steels with molten nitrate salt at 565˚C[16].

Alloy	Reaction	ΔG°(kJ/mol) 25˚C 1atm	ΔG(kJ/mol) 565˚C (838K)	
			AISI 321	AISI 347
Fe_2O_3	$2Fe+1.5O_2= Fe_2O_3$	-742.2	-721.276	-721.24
Fe_3O_4	$3Fe+2O_2=Fe_3O_4$	-1015.5	-1015.5	-986.83
Cr_2O_3	$2Cr+1.5O_2=Cr_2O_3$	-1058	-1018.658	-1018.549
NiO	$Ni+0.5O_2=NiO$	-211.7	-189.520	-189.75

4. Conclusion

In this study, the corrosion behaviours of the AISI 321 and 347 were experimentally investigated under isothermal (at 565˚C), thermal cycling (between 290 - 565˚C) and thermal shock (565˚C - 30˚C) at air atmosphere using a combination of gravimetric corrosion method and advanced surface and subsurface characterisation techniques. Here are the key conclusions from this study.

1. Thermal shock causes a higher rate of material loss than isothermal and thermal cycling heating profiles. This is linked to the effect of the synergy of substantial cyclic thermal stress and electrochemical activities on the resilience of the metal – molten salt interface.
2. The higher corrosion rate under thermal shock is also contributed to by the effect of the synergy of substantial cyclic thermal stress and electrochemical activities on the protective properties and/or rate of spallation interfacial oxide layers. The damage and spallation behaviours of the protective oxides layer were attributed to the stress mismatch between the bulk material and oxide layers across the interface, and linked to difference in the thermal expansion coefficient. The electrochemical activities are related to redox and/or chemical reactions that drives evolution of interfacial oxides and their dissolution.
3. The corrosion of AISI 321 and 347 under different thermal cycles follows this order in decreasing corrosion rates; thermal shock > isothermal > thermal cycling. The corrosion rate decreases with increase of immersion time under isothermal and thermal cycling, which is due to the resilience of the interfacial oxide layer and relative to test under thermal shock condition.
4. Results from this study suggests that the “thermal cycling” conditions suppresses corrosion kinetics which has always been considered as a corrosion-accelerate factor. Therefore stainless steel samples AISI 321 and AISI 347 can be considered as strong candidates to meet the down-selection requirement for use in hot tank and pipes for solar thermal energy storage system under isothermal and thermal cycling conditions. And the receiver pipes should consider using more corrosion-resistant Ni-based alloys, which are likely to suffer from the thermal shock. Note that this conclusion is limited by the results from a 4-week experiment.

5. The evolution in the chemistry of interfacial corrosion oxides was also affected by the different thermal cycles investigated. This is related to the effect of thermal cycles on the diffusion of species across the corrosion interface, kinetics of corrosion and oxide formation.

Declaration of competing interest

The authors declared that they have no conflicts of interest to this conflict of interest to this manuscript.

Acknowledgements

Dedicated to Late Prof. Anne Neville. OBE, FREng, FRS, FRSE, RAEng Chair in Emerging Technologies, University of Leeds

Special thanks to Dr Stuart Micklethwaith and Dr. Zebeada Aslam in LEMAS for their help on FIBs, TEM and SEM surface observation. The authors acknowledge the funding and support from Zhejiang JIULI Hi-tech Metals Co., Ltd through the Jiuli Hi-tech Metals Co – University of Leeds corrosion integrated centre.

Data Availability

The raw/processed data required to reproduce these findings will be made available on request.

CRediT authorship contribution statement

Qingyang Liu: Conceptualization, Methodology, Formal analysis, Investigation, Resources, Writing - original draft. **Jiong Qian**: Review & editing. **Anne Neville**: Resources & Supervision. **Frederick Pessu**: Supervision, Methodology, Writing - review & editing, Resources, Conceptualization.

References

[1] W. Ding, T. Bauer, Progress in Research and Development of Molten Chloride Salt Technology for Next Generation Concentrated Solar Power Plants, Engineering, 7 (2021) 334-347.

[2] M. Walczak, F. Pineda, Á.G. Fernández, C. Mata-Torres, R.A. Escobar, Materials corrosion for thermal energy storage systems in concentrated solar power plants, Renewable and Sustainable Energy Reviews, 86 (2018) 22-44.

[3] U. Pelay, L. Luo, Y. Fan, D. Stitou, M. Rood, Thermal energy storage systems for concentrated solar power plants, Renewable and Sustainable Energy Reviews, 79 (2017) 82-100.

[4] A.G. Fernández, J. Gomez-Vidal, E. Oró, A. Kruizenga, A. Solé, L.F. Cabeza, Mainstreaming commercial CSP systems: A technology review, Renewable Energy, 140 (2019) 152-176.

[5] G. Alva, Y. Lin, G. Fang, An overview of thermal energy storage systems, Energy, 144 (2018) 341-378.

[6] E. González-Roubaud, D. Pérez-Osorio, C. Prieto, Review of commercial thermal energy storage in concentrated solar power plants: Steam vs. molten salts, Renewable and Sustainable Energy Reviews, 80 (2017) 133-148.

[7] K. Vignarooban, X. Xu, A. Arvay, K. Hsu, A.M. Kannan, Heat transfer fluids for concentrating solar power systems – A review, Applied Energy, 146 (2015) 383-396.

[8] G. Mohan, M.B. Venkataraman, J. Coventry, Sensible energy storage options for concentrating solar power plants operating above 600 °C, Renewable and Sustainable Energy Reviews, 107 (2019) 319-337.

[9] S. Bell, T. Steinberg, G. Will, Corrosion mechanisms in molten salt thermal energy storage for concentrating solar power, Renewable and Sustainable Energy Reviews, 114 (2019).

[10] M. Elbakhshwan, D.H. Lee, M. Anderson, Corrosion resistance of high nickel alloys in solar salt at 600 °C for up to 4000 h, Solar Energy Materials and Solar Cells, 245 (2022) 111837.

[11] H. Li, X. Feng, X. Wang, X. Yang, J. Tang, J. Gong, Impact of temperature on corrosion behavior of austenitic stainless steels in solar salt for CSP application: An electrochemical study, Solar Energy Materials and Solar Cells, 239 (2022) 111661.

[12] Q. Gao, Y. Lu, Q. Yu, Y. Wu, C. Zhang, R. Zhi, High-temperature corrosion behavior of austenitic stainless steel in quaternary nitrate molten salt nanofluids for concentrated solar power, Solar Energy Materials and Solar Cells, 245 (2022) 111851.

[13] Q. Liu, R. Barker, C. Wang, J. Qian, A. Neville, F. Pessu, The corrosion behaviour of stainless steels and Ni-based alloys in nitrate salts under thermal cycling conditions in concentrated solar power plants, Solar Energy, 232 (2022) 169-185.

[14] R.W. Bradshaw, S.H. Goods, Corrosion resistance of stainless steels during thermal cycling in alkali nitrate molten salts, in, Sandia National Laboratories, 2001.

[15] B.-r. Li, H. Tan, Y. Liu, Q. Liu, G.-q. Zhang, Z.-f. Deng, G.-z. Xu, Y.-q. Guo, X.-z. Du, Experimental investigations on the thermal stability of Na2CO3–K2CO3 eutectic salt/ceramic composites for high temperature energy storage, Renewable Energy, 146 (2020) 2556-2565.

[16] Q. Liu, J. Qian, R. Barker, C. Wang, A. Neville, F. Pessu, Effect of thermal cycling on the corrosion behaviour of stainless steels and Ni-based alloys in molten salts under air and argon, Solar Energy, 238 (2022) 248-257.

[17] A. Mallco, F. Pineda, M. Mendoza, M. Henriquez, C. Carrasco, V. Vergara, E. Fuentealba, A.G. Fernandez, Evaluation of flow accelerated corrosion and mechanical performance of martensitic steel T91 for a ternary mixture of molten salts for CSP plants, Solar Energy Materials and Solar Cells, 238 (2022) 111623.

[18] C. Prieto, J. Ruiz-Cabañas, V. Madina, A.I. Fernández, L.F. Cabeza, Lessons learned from corrosion of materials with molten salts during molten salt tank preheating, Solar Energy Materials and Solar Cells, 247 (2022) 111943.

[19] J. Preußner, W. Pfeiffer, E. Piedra, S. Oeser, M. Tandler, P. Von Hartrott, C. Maier, Long-term material tests in liquid molten salts, in: Advances in Materials Technology for Fossil Power Plants - Proceedings from the 8th International Conference, 2016, pp. 1126-1137.

[20] P. Ramos, R.S. Coelho, F. Soldera, H.C. Pinto, F. Mücklich, P. Brito, Residual stress analysis in thermally grown oxide scales developed on Nb-alloyed refractory austenitic stainless steels, Corrosion Science, 178 (2021) 109066.

[21] N. Li, J. Xiao, N. Prud'homme, Z. Chen, V. Ji, Residual stresses in oxide scale formed on Fe–17Cr stainless steel, Applied Surface Science, 316 (2014) 108-113.

[22] N. Birks, G.H. Meier, F.S. Pettit, Introduction to the high temperature oxidation of metals, Cambridge university press, 2006.

[23] A. Fattah-alhosseini, S. Vafaeian, Comparison of electrochemical behavior between coarse-grained and fine-grained AISI 430 ferritic stainless steel by Mott–Schottky analysis and EIS measurements, Journal of Alloys and Compounds, 639 (2015) 301-307.

[24] A. G1-03, Standard Practice for Preparing, Cleaning, and Evaluating Corrosion Test Specimens, in, ASTM International, West Conshohocken，PA, 2017.

[25] B. Pieraggi, Calculations of parabolic reaction rate constants, Oxidation of Metals, 27 (1987) 177-185.

[26] K. Morshed-Behbahani, P. Najafisayar, M. Pakshir, M. Shahsavari, An electrochemical study on the effect of stabilization and sensitization heat treatments on the intergranular corrosion behaviour of AISI 321H austenitic stainless steel, Corrosion Science, 138 (2018) 28-41.

[27] Q. Liu, J. Qian, R. Barker, C. Wang, A. Neville, F. Pessu, Application of double loop electrochemical potentio-kinetic reactivation for characterizing the intergranular corrosion susceptibility of stainless steels and Ni-based alloys in solar nitrate salts used in CSP systems, Engineering Failure Analysis, 129 (2021) 105717.

[28] J.C. Gomez-Vidal, Corrosion resistance of MCrAlX coatings in a molten chloride for thermal storage in concentrating solar power applications, npj Materials Degradation, 1 (2017).

[29] A.G. Fernández, L.F. Cabeza, Corrosion monitoring and mitigation techniques on advanced thermal energy storage materials for CSP plants, Solar Energy Materials and Solar Cells, 192 (2019) 179-187.

[30] J. Slusser, J. Titcomb, M. Heffelfinger, B.J.J. Dunbobbin, Corrosion in molten nitrate-nitrite salts, 37 (1985) 24-27.

[31] O. Ahmed, Corrosion behaviour of AISI 304 stainless steel in contact with eutectic salt for concentrated solar power plant applications, (2013).

[32] X. Zhang, C. Zhang, Y. Wu, Y. Lu, Experimental research of high temperature dynamic corrosion characteristic of stainless steels in nitrate eutectic molten salt, Solar Energy, 209 (2020) 618-627.

[33] L. Ma, C. Zhang, Y. Wu, Y. Lu, Comparative review of different influence factors on molten salt corrosion characteristics for thermal energy storage, Solar Energy Materials and Solar Cells, 235 (2022) 111485.

[34] Á.G. Fernández, L.F. Cabeza, Molten salt corrosion mechanisms of nitrate based thermal energy storage materials for concentrated solar power plants: A review, Solar Energy Materials and Solar Cells, 194 (2019) 160-165.

[35] T.M. Besmann, N. Kulkarni, K. Spear, J. Vienna, Predicting Phase Equilibria of Spinel-Forming Constituents in Waste Glass Systems, in: Environmental Issues and Waste Management Technologies in the Ceramic and Nuclear Industries X: Proceedings of the 106th Annual Meeting of The American Ceramic Society, Indianapolis, Indiana, USA 2004, John Wiley & Sons, 2012, pp. 121.

[36] S. Goods, R. Bradshaw, M. Prairie, J. Chavez, Corrosion of stainless and carbon steels in molten mixtures of industrial nitrates, in, Sandia National Lab.(SNL-CA), Livermore, CA (United States), 1994.

[37] R.W. Bradshaw, S.H. Goods, Corrosion of alloys and metals by molten nitrates, in, Sandia National Lab.(SNL-CA), Livermore, CA (United States), 2001.

[38] W. Kai, C.C. Li, F.P. Cheng, K.P. Chu, R.T. Huang, L.W. Tsay, J.J. Kai, The oxidation behavior of an equimolar FeCoNiCrMn high-entropy alloy at 950°C in various oxygen-containing atmospheres, Corrosion Science, 108 (2016) 209-214.

[39] Q. Tan, N. Mo, B. Jiang, F. Pan, A. Atrens, M.-X. Zhang, Combined influence of Be and Ca on improving the high-temperature oxidation resistance of the magnesium alloy Mg-9Al-1Zn, Corrosion Science, 122 (2017) 1-11.

[40] Y. Yin, Q. Tan, Y. Zhao, Q. Sun, Z. Shi, M. Bermingham, W. Zhuang, H. Huang, M.-X. Zhang, A cost-effective Fe-rich compositionally complicated alloy with superior high-temperature oxidation resistance, Corrosion Science, 180 (2021) 109190.

[41] C. Wagner, Theoretical analysis of the diffusion processes determining the oxidation rate of alloys, Journal of the electrochemical Society, 99 (1952) 369.

[42] R. Lobnig, H. Schmidt, K. Hennesen, H. Grabke, Diffusion of cations in chromia layers grown on iron-base alloys, Oxidation of Metals, 37 (1992) 81-93.